Changes in intra-nuclear mechanics in response to DNA damaging agents revealed by time-domain Brillouin micro-spectroscopy

Liwang Liu, Marina Simon, Giovanna Muggiolu, Florent Vilotte, Mikael Antoine, Jerôme Caron, Guy Kantor, Philippe Barberet, Hervé Seznec, Bertrand Audoin

Photoacoustics 27 (2022) 100385

Contents lists available at ScienceDirect

Photoacoustics

journal homepage: www.elsevier.com/locate/pacs

Changes in intra-nuclear mechanics in response to DNA damaging agents revealed by time-domain Brillouin micro-spectroscopy

Liwang Liu [a,1], Marina Simon [b], Giovanna Muggiolu [b], Florent Vilotte [b,c], Mikael Antoine [c], Jerôme Caron [c], Guy Kantor [c], Philippe Barberet [b], Hervé Seznec [b], Bertrand Audoin [a,*]

[a] Univ. Bordeaux, CNRS, I2M, UMR 5295, F-33400 Talence, France
[b] Univ. Bordeaux, CNRS, CENBG, UMR 5797, F-33170 Gradignan, France
[c] Department of Radiotherapy, Institut Bergonié, Comprehensive Regional Cancer Centre of Bordeaux and Southwest and University of Bordeaux, France

ARTICLE INFO

Keywords:
DNA damage/repair
Chromatin condensation/decondensation
Molecular clustering
Nuclear mechanics
Coherent phonon spectroscopy
Picosecond ultrasonics
Ultrafast opto-acoustics

ABSTRACT

How DNA damage and repair processes affect the biomechanical properties of the nucleus interior remains unknown. Here, an opto-acoustic microscope based on time-domain Brillouin spectroscopy (TDBS) was used to investigate the induced regulation of intra-nuclear mechanics. With this ultrafast pump-probe technique, coherent acoustic phonons were tracked along their propagation in the intra-nucleus nanostructure and the complex stiffness moduli and thicknesses were measured with an optical resolution. Osteosarcoma cells were exposed to methyl methanesulfonate (MMS) and the presence of DNA damage was tested using immunodetection targeted against damage signaling proteins. TDBS revealed that the intra-nuclear storage modulus decreased significantly upon exposure to MMS, as a result of the chromatin decondensation and reorganization that favors molecular diffusion within the organelle. When the damaging agent was removed and cells incubated for 2 h in the buffer solution before fixation the intra-nuclear reorganization led to an inverse evolution of the storage modulus, the nucleus stiffened. The same tendency was measured when DNA double-strand breaks were caused by cell exposure to ionizing radiation. TDBS microscopy also revealed changes in acoustic dissipation, another mechanical probe of the intra-nucleus organization at the nano-scale, and changes in nucleus thickness during exposure to MMS and after recovery.

1. Introduction

Gene integrity is continuously challenged by DNA lesions caused by normal metabolic activities or environmental factors. In the event of a DNA break, the cell activates DNA damage response pathways that allow detection and repair of the lesion. Failures to repair are important sources of genome instability, giving rise to chromosomal aberrations and severe biological consequences including tumorigenesis and cell death [1,2]. Although studies have been conducted to explore changes in the physical organization of the nucleus in response to DNA damage [3–5], the description remains incomplete mainly due to the limitation of the existing technologies [6,7]. However, research has shown that both DNA damage and repair lead to the activation of different biochemical pathways and to major nuclear reorganization, for which alteration of the nucleus mechanics has been increasingly recognized as the hallmark event [8–10]. Direct measurement of the mechanical behavior of the interior of the nucleus is thus expected to give a better understanding of the structural changes that accompany the cell response to DNA damage.

DNA is mainly packed in compacted histone-DNA complexes forming nucleosomes, the building blocks of chromatin. Through epigenetic regulation, chromatin can be packaged into different conformations and higher-order structures that modulate gene expression and access of transcription factors to their binding sites [11,12]. Chromatin compaction thus prevents DNA damage and determines the accessibility of DNA to the repair machinery [3,4,7]. Chromatin fiber is the main component of the nucleus interior. It has been identified as the major load-bearing element of the nucleus [12,13], and the chromatin condensation state has been shown to dictate nuclear stiffness [14–17]. Moreover, it has been demonstrated *in vitro* and in living cells that the self-association of nucleosomal arrays produces supramolecular condensates in which the chromatin is physically constrained and solid-like. This solid-like

* Corresponding author.
E-mail address: bertrand.audoin@u-bordeaux.fr (B. Audoin).
[1] Present Address: Now at KU Leuven, Department of Physics and Astronony, Celestijnenlaan 200D, BE-3001 Leuven, Belgium.

https://doi.org/10.1016/j.pacs.2022.100385
Received 29 April 2022; Received in revised form 5 July 2022; Accepted 8 July 2022
Available online 11 July 2022

behavior stands even under conditions that produce limited interactions between chromatin fibers. Chromatin networking thus provides a solid scaffold that resists external forces and supports liquid-liquid phase separation and chromatin binding proteins [18].

Although chromatin relaxation and reorganization following DNA damage have been documented, very little is known about how this impacts nuclear structure and mechanics. The challenge encountered with the existing contact-based measurement techniques of the nuclear mechanics is the masking effect that the stiff cytoskeletal fibers around the nucleus have on measurements. Because of this, many studies resort to the use of isolated nuclei by removing the cytoskeleton entirely [7, 19]. The physiological environment is then lost and, moreover, the mechanics of the probed nucleus is then primarily governed not by the chromatin but rather by the nuclear lamina, a dense complex meshwork of proteins less than 100 nm thick that resides between the nuclear membrane and the chromatin. A new methodology that allows the in-depth study of the nucleus interior is thus required to understand how the changes in chromatin organization, that accompany DNA damage and repair, influence the mechanical behavior of the nucleus [7].

In this work, we present an ultrafast opto-acoustic pump-probe technique to launch and record the propagation of GHz coherent acoustic phonons (CAPs) inside cell nuclei. Using this entirely optical mean we measure in time-domain the Brillouin frequency shift that results from the interaction of the probe light pulses with the plane acoustic wavefront propagating in the chromatin domain. The CAPs' velocity and attenuation are analyzed in terms of a complex longitudinal modulus, with the storage modulus depending primarily on the chromatin compaction and conformation and the loss modulus revealing dissipation due to fiber flexibility or scattering by in-homogeneities of a size close to the phonon wavelength.

We induced DNA damage in sarcoma cells by exposing them to a DNA alkylating agent for different exposure times. We performed immunodetection to image the damage foci and quantified their numbers. The changes in the complex longitudinal modulus inside the nuclei were measured with cells fixed after exposure and 2 h after the damaging agent was removed. The mechanical changes caused by the nanostructure reorganization were also measured when the DNA damage was induced using ionizing radiation. We demonstrate the sensitivity of time-domain Brillouin spectroscopy to changes in the viscoelastic properties of the intra-nucleus induced by the damaging agents and during recovery.

This novel label-free microscopy modality provides unique insights into the biomechanics of DNA damage and recovery. It allows us to probe the intra-nuclear mechanics remotely and as such it opens up new research avenues into the physical organization of the nuclear chromatin.

2. Materials and methods

2.1. Pump-probe opto-acoustic microscope

In this work, the all-optical tracking of coherent acoustic phonons (CAPs) was carried out by using the setup shown in Fig. 1a. A compact dual-oscillator (t-Pulse Duo, Amplitudes Systemes®), containing two passively mode-locked Yb: KYW laser cavities, emits two trains of laser pulses (400 fs) with one serving as the pump (1030 nm) and the other as the probe (515 nm). The two laser pulses are operated at approximately $f_0 = 48$ MHz, while with a slight shift, Δf, between the two repetition frequencies to achieve asynchronous optical sampling (ASOPS). Δf is generated by a frequency synthesizer and is stabilized at 2 kHz using an active feedback loop. In such a configuration, a time delay of ~20 ns, reciprocal of f_0, is scanned within 500 μs, reciprocal of Δf, with a time resolution of 870 fs, without involving any mechanical scanning, *e.g.* in a mechanical delay line. Hence, this scheme avoids several intrinsic drawbacks encountered in the conventional mechanically-controlled delays scanning, for instance, beam pointing fluctuation, modifications of the size of the focal spot on the sample, and long acquisition time. The two beams are coaxially aligned and focused by an objective lens, x 50 (beam diameter is approximately 1.0 μm), through a sample (cell) onto the surface of a Ti plate, which is situated on a translation stage (PI5633D, Physik Instrumente®), thus allowing the 1D and/or 2D scanning of the sample with a high precision down to 2 nm. At the

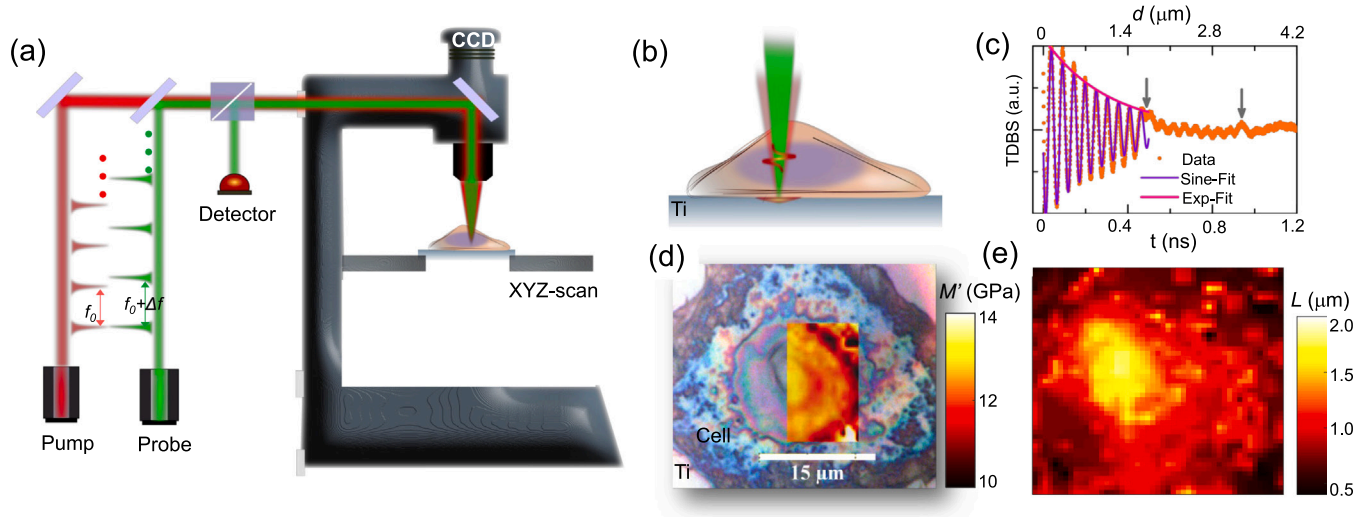

Fig. 1. Principle of TDBS microscopy of nucleus viscoelastic properties and thickness. (a) Pump and probe laser beams are integrated into a commercial reflected-light bright-field microscope. TDBS uses the asynchronous optical sampling technique where a pair of fs-oscillators are operated at slightly different repetition rates, f_0 (48 MHz) and $f_0 + \Delta f$ (2 kHz). In such a configuration, a time delay of ~20 ns, reciprocal of f_0, is scanned within 500 μs, reciprocal of Δf, with a time resolution of 870 fs, without involving any mechanical scanning. (b) Cells are cultured on a Titanium (Ti) opto-acoustic transducer. Absorption of the pump pulse in Ti leads to the generation of coherent acoustic phonons through the transient thermoelastic effect, hence amplifying the Brillouin scattering signal detected by the probe pulses. (c) Representative TDBS waveform (dots) acquired in the cell nucleus of an osteosarcoma cell. It is fitted by a damped sine wave to extract the frequency (purple) and attenuation (pink) of the time-domain Brillouin oscillations. Arrows show the moment when the CAPs reach the boundary of the cell nucleus. (d) By scanning the coaxially aligned pump and probe beams, the mechanical properties, averaged through the nucleus thickness, can be mapped with a diffraction-limited 1 μm resolution, as illustrated with the overlay of the optical image of an osteosarcoma cell with the image of the bulk longitudinal storage modulus, M', measured in the nucleus region. (e) The thickness, L, in the nuclear region is also extracted by processing the TDBS signals.

sample/Ti interface, each pump pulse launches a longitudinal strain pulse, which alters the intensity of the reflected probe light during its propagation. The resulting intensity variation of the probe light is monitored by a photodetector (PDB440A, Thorlabs®) in connection with a 14-bit digitizer (PXI-5122, National Instruments®). The data readout and averaging is done by homemade Labview (National Instruments®) programmes installed on a computer that communicates with the digitizer via a GPIB interface. During measurements, low pump and probe powers at 3 mW and 1 mW, respectively, were used to avoid any possible photo-damage to the cells. Power was measured by a power meter (1917-R, Newport®) placed just beneath the objective lens. Thanks to the high acquisition speed of ASOPS configuration, this setup can determine optical reflectivity changes as small as 10^{-5} within approximately 5 s. This yields 12 pixels per minute in a raster scan fashion. Another notable feature of this setup is its high compatibility with other commonly used microscopic methods. In this setup, the main apparatus involved in the PU detection are accommodated in a commercial reflected light microscope (BXFM-F, Olympus®). By translating the switchable mirrors allocated between the objective nosepiece and the filter cube, it is simple to switch the function of the setup between PU microscopy, using the 100 % reflection mirror, and reflected field microscopy, using the 50 % or the 100 % transmission mirror. This gives not only precise alignment of the laser beams onto a target cell but also convenient access to other microscopic knowledge of the cell under inspection.

2.2. Cell culture and cell preparation

Osteosarcoma cell line (HTB96 U2OS, ATCC) was maintained in McCoy's 5 A Medium supplemented with Fetal Bovine Serum (10 % v/v, FBS) and streptomycin/penicillin (100 μg/ml). Cells were kept in a humidified atmosphere at 37 °C and 5 % (v/v) CO_2. For both chemical treatment and irradiation experiments 20,000 cells were drop-seeded in specific cell dishes 20 h before treatment. A mock sample was used as a control, which was treated in the same way with the exception of the DNA-damaging treatment. For opto-acoustic measurements, cells were plated on Ti plates and treated with paraformaldehyde as for the immunodetection protocol. Once fixed, cells were rinsed with PBS (pH 7.4) and kept in ethanol 70 % (v/v) at + 4 °C.

2.3. Methyl methanesulfonate (MMS) treatment

MMS was dissolved in dimethyl sulfoxide just before use. Treatments with MMS were performed in McCoy's 5 A Medium supplemented with serum and antibiotics. All solutions were prepared just before treatment. MMS was used at a concentration of 1.5 mM with different exposure times (3 min, 30 min, 3 h, and 8 h).

2.4. Irradiation

6 MV medical X-Rays irradiations were performed with a Clinical Linear Accelerator (CLINAC, Varian Medical Systems), routinely in use at the Department of Radiotherapy, Institut Bergonié (Bordeaux, France). Cells were irradiated using 6 MV X-Rays beams with 2 and 6 Gy delivered at a dose-rate of 2 Gy/min. Cells were plated on glass coverslips or on Ti plates. The cell monolayer was covered by 15 mm of medium to achieve electronic equilibrium. The X-ray beam was collimated to a 15 × 15 cm^2 square field. The irradiations were carried out with a single beam oriented at 0° (single vertical beam). Coverslips or Ti plates were immersed in 9.6 ml of growth medium (McCoy's 5 A) in a 6-well plate.

2.5. Immunodetection

The co-immunostaining of **γH2A.X** and P-ATM was performed following the protocols described by Bennett et al [20]. Briefly, after exposure, cells were paraformaldehyde-fixed (4 % w/v) in PBS for 15 min at room temperature. Then, cells were incubated using a blocking buffer (Triton X-100, 0.2 % v/v and FBS, 10 % v/v in PBS) for 30 min at room temperature. After three washes in PBS for 5 min, samples were incubated overnight, at 4 °C with anti-human **γH2A.X** rabbit monoclonal antibody (1:1000, 20E3, *Cell Signaling*). After three more washes in PBS, samples were incubated for 3 h at room temperature with goat anti-rabbit conjugated to Alexa $Fluor^{488}$ antibody (1:2000 Molecular Probes, *Invitrogen*). The same process was repeated with anti-human P-ATM mouse monoclonal antibody (1:1000, 10H11. E12, *Cell Signaling*), and goat anti-mouse conjugated to Alexa $Fluor^{594}$ antibody (1:2000, Molecular Probes, *Invitrogen*). Nuclei were stained with $Hoechst^{33342}$ (1 μM, 10 min at room temperature). Image acquisition was performed using a Carl Zeiss fluorescent microscope with a 63X/Oil immersion objective. The number of foci was counted in 40–60 cells per condition with a custom-made Image J macro [21].

3. Results

3.1. Time-domain Brillouin micro-spectroscopy (TDBS)

TDBS [22,23] is an all-optical and label-free modality that allows the remote measurement of the cell nucleus' mechanical properties. It relies on the ultrafast pump-probe spectroscopy of the interaction of light with optically launched GHz coherent acoustic phonons (CAPs). By implementing TDBS in a reflected light microscope, shown schematically in Fig. 1a, we developed a Brillouin pulsed opto-acoustic microscope (B-POM) that enables the microscopic quantitative imaging of both nucleus elasticity and nucleus thickness. To achieve microscopy of the cell viscoelasticity cells were cultured on the surface of a titanium plate serving as a biocompatible opto-acoustic transducer that boosted the generation of CAPs in cells upon absorption of the pump light by the metal, Fig. 1b [24]. Hence it actively generated the Brillouin scattering measured within the cell by the probe light. This is one feature that distinguishes TDBS from conventional Brillouin light spectroscopy (BLS), which is based on passive detection of the spontaneous Brillouin scattering arising from weak incoherent phonons [25–28]. In TDBS, the scattering occurs throughout the coherent propagation of the transient acoustic phonons in the cell nucleus. The beating, at a GHz frequency, of the scattered light with the reflection of the probe light at an interface in the sample was monitored with sub-picosecond time resolution using the asynchronous optical sampling technique [29]. Fig. 1c presents a typical waveform (blue) measured in the nucleus of an osteosarcoma cell. It is characterized by a damped sinusoid at the so-called Brillouin frequency $f_B = 2n\nu/\lambda$, in the case of normal incidence, with n the refractive index of the cell nucleus, ν the longitudinal sound velocity of CAPs, and λ the light wavelength of the probe laser, 515 nm in this work. Fitting the measured waveform with a damped sinusoid, as illustrated with the pink and purple curves in Fig. 1c, is convenient to extract the frequency f_B and lifetime τ of the Brillouin oscillations. The two quantities are related to the intra-nuclear elasticity and losses, respectively. From the general equation governing the acoustic propagation in a viscoelastic medium, the complex modulus M^* can be expressed by:

$$M^* = M' + iM'' = \rho v^2 + i\frac{\rho v^2}{\pi f_B \tau} \quad (1)$$

with the real and imaginary parts describing the longitudinal storage and loss moduli, respectively. TDBS measurements can therefore be used to assess the complex modulus, given the known mass density, ρ, and optical refractive index, n, of the sample [30]. Moreover, the presence of a stepwise signature in the measured waveform, as labeled with arrows in Fig. 1c, marks the moment when the CAPs reach the top surface of the cell nucleus. With the pre-determined sound velocity, one can thus simultaneously obtain the nucleus thickness, as illustrated with the top axis in Fig. 1c. This is another difference between TDBS and

conventional Brillouin spectroscopy, where thickness information is not accessible. A detailed description of the procedures involved in extracting the nucleus complex modulus and thickness is presented in the data processing section in Supplementary Information (SI).

The lateral resolution in the TDBS imaging is inherently limited by optical diffraction: down to submicron can be achieved using high-magnification objective lenses. In this work, we used a 50x-objective to yield a lateral resolution of ~ 1.0 μm. It was therefore possible to collect a large amount of signal in a single nucleus, which typically has a diameter of around 10–15 μm, an usual size for osteosarcoma. Online movie 1 shows changes in the probe reflectivity for 418 ps at a frame rate of ≈ 2 fr/ps. As an example, Fig. 1d presents the overlay of the optical image of an osteosarcoma cell, provided by the built-in reflected light microscope, with one acoustic image showing the mapping of the storage modulus, M', through the thickness of cell, in the nuclear region. By further processing the TDBS signals, maps of thickness L can also be obtained in the nuclear region, as shown in Fig. 1e.

3.2. Methyl methanesulfonate (MMS) and radiation-induced DNA damages

A routinely used DNA alkylating agent, MMS was used to induce DNA damage to sarcoma cells. MMS has been used for many years for this purpose. It modifies both guanine (to 7-methylguanine) and adenine (to 3-methlyladenine) to cause base mispairing and replication blocks, respectively [31]. DNA damage caused by alkylating agents is predominantly repaired by the base excision repair pathway and DNA alkyl transferases [32]. We treated sarcoma cells with MMS at several exposure times: 3 min, 30 min, 1, 3, and 8 h. After exposure, cells were thoroughly rinsed with the buffer solution containing no MMS to remove residual traces. Cells not subjected to MMS exposure were reserved as control (CT) samples for comparisons. Sarcoma cells were also exposed to ionizing radiation (IR) to inflict radiation-induced DNA damage.

In order to validate the efficacy of the MMS treatment and radiation exposure conditions, we tested the presence of DNA damage by using immunodetection targeted against the specific phosphorylated form of DNA damage signaling proteins (**H2A.X** and ATM). Cells were paraformaldehyde-fixed and treated with antibodies targeted against the phosphorylated form of **H2A.X** isoform, named **γH2A.X** (phosphorylation on serine 139) and ATM (phosphorylation on serine 1981) [33]. Histone **H2A.X** is rapidly phosphorylated in the chromatin microenvironment surrounding a DNA double-strand break (DSB), where it recruits repair and checkpoint protein complexes. **γH2A.X** foci formation is considered to be a sensitive and selective signal for the

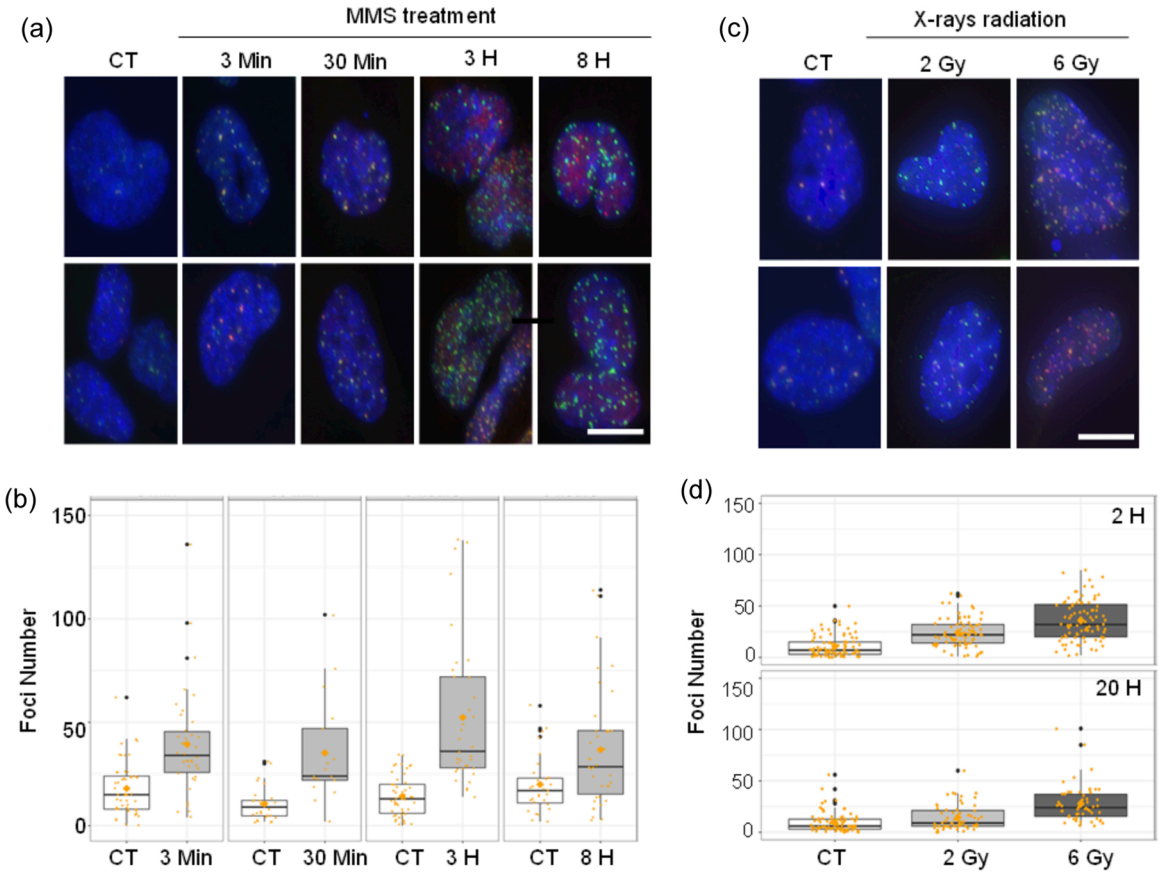

Fig. 2. **γH2A.X** and P-ATM foci in sarcoma cells treated with methyl methanesulfonate (MMS) or exposed to ionizing radiation (IR). (a). Immunodetection performed on fixed cells immediately after MMS treatment. Cells were incubated in the presence of MMS at 1.5 mM for 3 min, 30 min, 3 h and 8 h, respectively. Top and bottom rows show several cells for each condition. Control cells show a weak presence of foci in the cell nuclei for both phosphorylated **H2A.X** (**γH2A.X**, green) and phosphorylated ATM (red). **γH2A.X** foci number increased with incubation time with MMS, with a maximum at 3 h. Nuclei (in blue) were stained with Hoechst[33342]. Scale bar 10 μm. (b) Quantification of **γH2A.X** foci in sarcoma cells immediately after MMS treatment. The number of foci is not related to incubation time. (c) Immunodetection of **γH2A.X** and P-ATM radiation-induced foci in sarcoma cells after 6 MV X-Rays exposures (2 and 6 Gy). Control cells show a weak presence of foci in the cell nuclei for both phosphorylated **H2A.X** (green) and ATM (red). 2 h after irradiation, irradiated cells show bright foci with increased diameter. Nuclei (in blue) were stained with Hoechst[33342]. Scale bar 10 μm. (d) Quantification of **γH2A.X** foci in sarcoma cells. The number of foci observed 2 and 20 h after irradiation depends on the dose delivered, and decreases over time in irradiated cells. In (b) and (d) data are shown with orange dots, box and whiskers indicate minimum, first quartile, third quartile and maximum, black line is for median, orange diamond is for mean value and black dots are for outliers. (For interpretation of the references to color in this figure legend, the reader is referred to the web version of this article.)

existence of DSB. As shown in Fig. 2a, the kinetics of **γH2A.X** foci formation showed rapid DSB formation for cells treated immediately after MMS treatment (1.5 mM for 3 min), whereas very few foci were detectable in control cells. Moreover, the double staining with **γH2A.X** and P-ATM revealed with their co-localization that they were DNA DSBs. The quantitative analysis, Fig. 2b, revealed a maximum of **γH2A.X** foci formation for 3 h MMS exposure.

We also irradiated cells with 6 MV X-Rays at doses of 2 and 6 Gy and tested the presence of radiation-induced DNA DSBs by immunodetection 2 and 20 h after irradiation. Control cells show a weak presence of foci in the cell nuclei for both phosphorylated **H2A.X** (green) and ATM (red), as illustrated in Fig. 2c. By contrast, irradiated cells show bright foci with increased diameter size and **γH2A.X** foci quantification revealed an increase in foci number with dose. We also show in Fig. 2d that the number of foci observed 2 and 20 h after irradiation is dependent on the dose delivered, and decrease over time after irradiation is observed.

3.3. *Changes in intra-nucleus mechanical properties following exposure to MMS and to ionizing radiation*

The acquisition time of a single signal with the TDBS technique, see Fig. 1(c), is of the order of seconds. Detection of fine mechanical changes requires statistics over a large number of data to be collected for several minutes. This is not compatible with the dynamics of the cell response to damage thus real-time evaluation was not possible. The dynamics of the response was thus sampled by fixing cells after several exposure durations. The effect of fixative on the mechanical changes we measured is detailed further in Section 4.1 where the assessing to the cell nanostructure with GHz phonons is discussed.

Three groups of samples were prepared, all with cells cultured on titanium plates to allow for opto-acoustic experiments, see Section 2. The first two groups included control samples and samples with cells exposed to MMS (1.5 mM) for 30 min, 1 h or 3 h.

Cells in the first group were immediately fixed with paraformaldehyde after MMS exposure, rinsed with phosphate buffer saline and dehydrated in ethanol (70 % v/v). We used B-POM to perform TDBS measurements and to evaluate remotely the intra-nuclear GHz viscoelastic properties, namely the storage modulus (M') and loss modulus (M''), and the nucleus thickness (L), see Supplementary Information (SI) for details on data processing. For each exposure time, numerous TDBS measurements were performed in the cell nuclei, in total 720 individual measurements out of 20 individual cells. For each cell, a 6 × 6 scan, 36 points, was carried out in the nucleus with a step of 1 μm. The statistical analysis of the measured moduli and thicknesses are presented in Fig. 3a-c with box-whisker plots, respectively. In these plots, the height of the box spans the first quartile to the third quartile. The horizontal line and the cross inside the box represent the median and the mean value, respectively. The top/bottom vertical lines represent the mean value plus/minus the standard deviation (1σ). A Kolmogorov–Smirnov test was performed to quantify the significance of differences between the measurements for MMS-treated samples and for control samples [34]. This test was chosen owing to the non-normal nature of the distributions of both the storage and loss moduli measurements. The test reveals that the differences with respect to the control samples are significant ($p < 0.001$) for all measurement statistics of M' and of M''. Moreover, monotonic changes according to exposure time are observed for both real and imaginary parts of the intra-nuclear viscoelastic coefficients. The mean value of the storage modulus decreased by as much as -7 ± 2 % [35] when cells were fixed immediately after exposure to MMS for 3 h, Fig. 3a. After MMS exposure, the distributions of the storage modulus values, M', clearly change from a normal distribution for the control samples to skewed distributions for MMS-treated samples, especially for the 30 min and 1 h exposure times, with the increasing number of data revealing a drastic decrease in the storage modulus. These results are in line with the kinetics of the **γH2A.X** foci formation showing rapid DSB formation and changes in the foci number from balanced to skewed when exposure time increases, Fig. 2b. The TDBS results also show that the mean loss modulus increases by up to 14

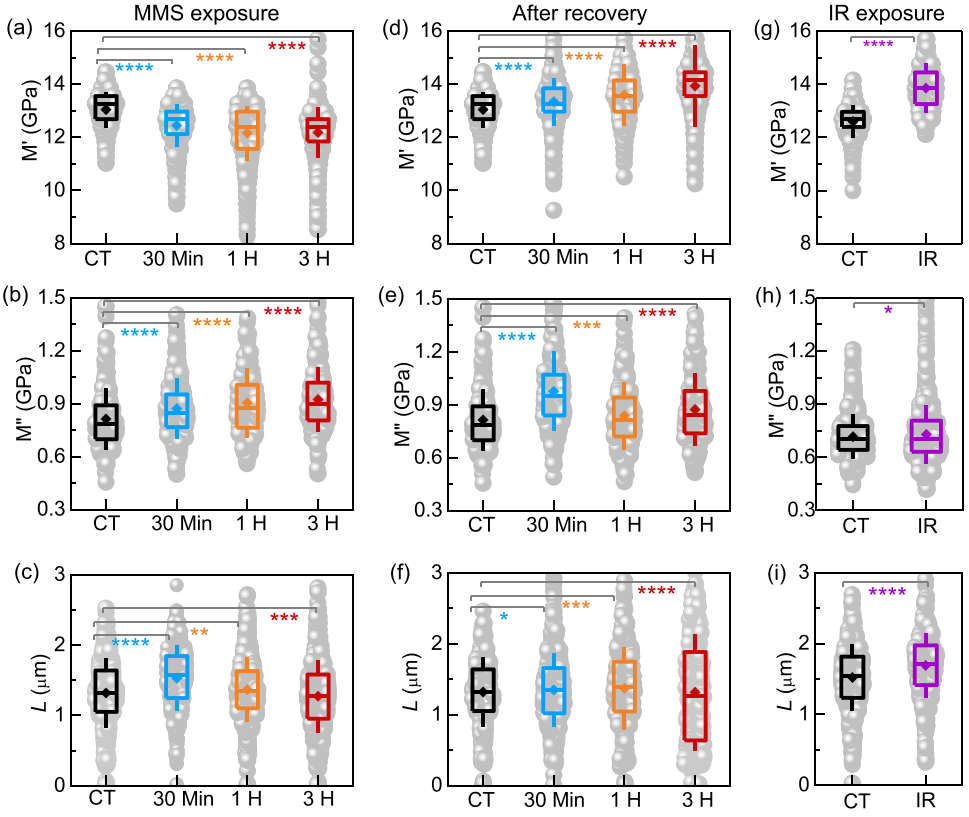

Fig. 3. Box-and-whisker plots of the TDBS measurements of intra-nucleus storage moduli M' and loss moduli M'', and of the nucleus thickness L. Each histogram includes 720 measurements from 20 individual cells. Number of stars indicates the significance of differences (p-value) according to a Kolmogorov-Smirnov test, * $p \leq 0.05$, * * $p \leq 0.01$, * * * $p \leq 0.001$, * * * * $p \leq 0.0001$. The first two columns are for cells exposed to MMS, with no recovery (a–c) and with 2 h′ recovery (d–f). The third column (g–i) shows results for cells exposed to IR and fixed 2 h after exposure. When cells are fixed after MMS exposure the intra-nucleus storage modulus decreases (a) as the exposure time increases. The opposite is measured when recovery was allowed for 2 h before cell fixation (d). The same increase in the storage modulus is measured for cells exposed to IR (g). The intra-nucleus loss modulus increases (b) upon increasing the exposure time to MMS when there is no recovery, while no clear tendency is measured in the recovery case, neither for MMS (e) nor for IR (h). No clear change in the nucleus thickness is measured by increasing the exposure time to MMS in the no-recovery case (c). However, the thickness becomes more dispersed when recovery was allowed after exposure to MMS (f), and greater when recovery was allowed after exposure to IR (h).

± 13 % [35] after exposure for 3 h and immediate fixation, Fig. 3b. The statistics for the nuclei thickness measurements however reveal less significant changes with respect to the control samples for long exposure times of 1 and 3 h, with greater p values meaning that thickness does not seem to change with respect to CT.

In addition to this analysis, which considers each sample in this first group as a whole, we performed a cell-by-cell analysis for each sample, thanks to the large number of intra-nuclear data we collected. We could then discuss the homogeneity of the changes in elastic moduli from one cell to another in the same batch, *i.e.* for each exposure time, and also the homogeneity of the changes inside nuclei. Results are given in the SI and the tendencies we found are discussed further on.

In a second group, MMS-treated cells were rinsed and incubated in their cell culture medium for 2 h before fixation. The same fixation and de-hydration protocols were used as for the cells in the first group. During this 2-hour period the DNA damage response may involve several factors such as cell mobility, cell shrinking, and cell death. In addition, the DNA repair pathways, which were activated for 3 min only after MMS exposure according to the immunodetection results, can be still active whereas the DNA damaging agent was removed.

Again, 720 individual TDBS measurements were conducted in 20 individual cells for the control sample and also for samples exposed to MMS. The statistics of the measured storage and loss moduli and thicknesses are presented in Fig. 3d-f. Regarding the storage modulus, we measured an opposite tendency compared to that obtained when cells were fixed immediately after exposure to MMS. Here, we recorded a significant monotonic increase in the mean storage modulus, up to 7 ± 2 % [35] when cells were exposed to MMS for 3 h, Fig. 3d. This effect is accompanied by a balancing of the data statistics showing that more cells have higher storage moduli.

No clear monotonic tendency could be found for the changes in loss moduli and no significant changes in the nuclei thicknesses with respect to CT were detected. However, we did notice an increase in Fig. 3f in the spreading of thickness data with respect to the control cells and also to cells fixed after exposure to the damaging agents, Fig. 3c, especially for cells exposed to MMS for 30 min. This spreading reveals an increase in the roughness of the nucleus surface. The B-POM has already proved its capability to measure greater nucleus roughness for abnormal cells than for healthy cells [36]. Nuclear herniations and blebbing are indeed cell phenotypes that have long been considered for some cancer diagnosis and for tumor grading [7,37]. Here, the globulated morphologies could be caused by chromatin relocation or chromatin remodeling [38] during recovery.

In Fig. 4a, we plot the relative changes in mean storage modulus, loss tangent and nucleus thickness with respect to their initial values as measured for CT, $\Delta X_t/X_0$ with $\Delta X_t = X_t - X_0$, where X stands for the mean of either the storage modulus, M', or the loss tangent M''/M', and the subscript denotes exposure time to MMS. Fig. 4b shows the relative changes in data measured after recovery. Here, the reference values we considered were not for CT but instead we used as reference the mean values we measured when cells were fixed immediately after exposure, *i.e.* counterparts of the same colors in Fig. 3. We thus plotted $\Delta X_{t|2|}/X_t$ with $\Delta X_{t|2|} = X_{t|2|} - X_t$, where $\Delta X_{t|2|}$ is the mean value measured after exposure for t and recovery for 2 h. Therefore Fig. 4b presents relative changes in these quantities during solely the recovery period of 2 h, as a function of the exposure time. Fig. 4 shows the relative changes of M' and M'' during exposure and during recovery do not evolve linearly with the exposure time. These distinct relative changes in mean values will be commented further on in the discussion section.

So far, we have presented the results we obtained by TDBS measurements for two different groups of cells treated by MMS. Remarkably, we obtained statistically significant changes in the intra-nucleus storage moduli with opposite tendencies. The cell nuclei are softened, compared to their control counterparts, when cells were fixed immediately after exposure to MMS, whereas they become stiffer when the cell response to DNA damage was not blocked after the DNA damaging agent was removed.

On the basis of these findings, we decided to investigate whether the B-POM could probe the mechanical changes in cell nuclei exposed to IR. Osteosarcoma cells in the third group we prepared were exposed to IR (6 MV X-Rays at 6 Gy) and incubated in the buffer solution for two hours before fixation, following the same protocol as for cells exposed to MMS.

TDBS measurements were performed in the nucleus of several cells from the control sample and from the sample exposed to IR. For each of these samples, 720 individual TDBS measurements were carried out on 20 individual cells. The results in terms of storage modulus, thickness, and loss modulus are illustrated in Fig. 3g-i, respectively. Clear nucleus stiffening is observed after irradiation and recovery for 2 h, with a 10 ± 2 % increase [39] in the mean storage modulus and a wider non-skewed distribution of the data, Fig. 3 g, whereas changes in the loss modulus are not significant, Fig. 3 h. We thus measured the same mechanical response as the one observed when cells were treated with MMS and kept in the buffer solution for 2 h after the damaging agent was removed, Fig. 3d-e. This is consistent with the immunodetection tests we presented previously, Fig. 2, showing similar damage foci numbers after MMS exposure and IR exposure. One can thus assume that the same processes may explain the stiffening measured after the recovery time.

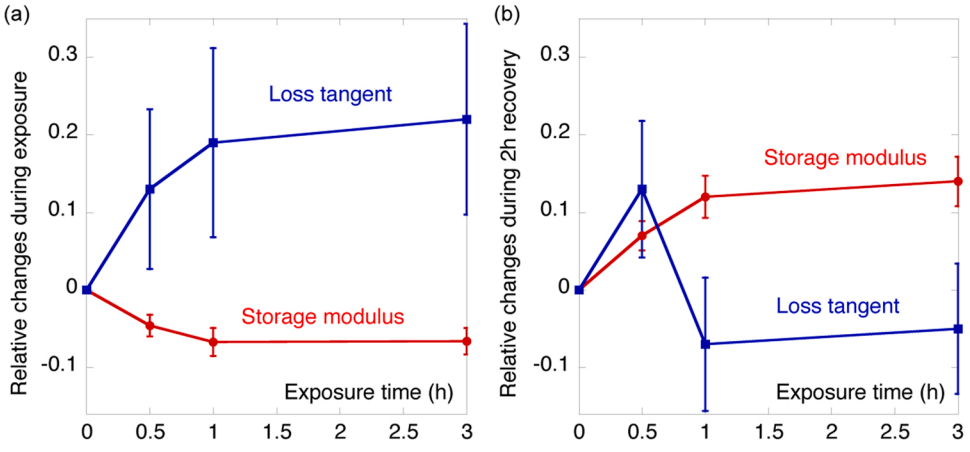

Fig. 4. Relative changes in mean storage modulus (red, circles) and loss tangent (blue, squares). (a) Relative changes, compared to CT, in mean values of data measured after exposure to MMS. (b) Relative changes in mean values of data measured after a 2-hour recovery. In this case, in order to represent cell activity during the recovery period only, relative changes are calculated with respect to data measured when cells were fixed immediately after exposure. Data and estimation of uncertainties are in SI.

4. Discussion

4.1. Probing the cell nanostructure with GHz phonons

We now briefly review some results, published earlier, showing connections between the complex storage modulus, as measured at GHz frequencies, and the nanostructure of cell sub-components. We then discuss our results in light of these works.

Brillouin light microscopy (BLM) [27,40,41], an emerging imaging technique based on BLS, has shown ability to provide the elasticity characteristics of nanostructured hydrogels at their mesoscale [42], and it could be applied to map the intracellular mechanical properties [43]. To investigate the sensitivity to liquid-solid regulation under different osmotic conditions, sucrose was added to the cell medium to generate osmotic pressure. A substantial linear increase in the cell elastic modulus was measured with the increase in sucrose concentration, attributed to an increase in the solid volume fraction inside the cell [44]. In addition, the sensitivity of the Brillouin shift to actin polymerization and to branching of actin fibres, two major mechanisms of cytoskeleton stiffening, was verified with actin gels *in vitro*; and in cells with the inhibition of the actin polymerization with cytochalasin D [43]. A decrease in cell stiffness was measured in the same way when cells were treated with latrunculin-A, a toxin that prevents polymerization of actin filaments [45]. Nuclear mechanics also, and notably the effect on it of chromatin decondensation, was investigated with BLM [17,46]. With this goal, cells were treated with Trichostatin A (TSA) to inhibit histone deacetylase and to cause chromatin decondensation [47]. In accordance with the softening measured previously with other means, the Brillouin shifts revealed a decrease in the nucleus longitudinal modulus with chromatin decondensation, *i.e.* when treated with TSA.

Evidence of sensitivity of TDBS to the nanostructure of the sub-cell components was first provided by experiments in the micron-thick wall of vegetal cells [48]. This wall is made of cellulose microfibrils embedded in a pectin matrix and its mechanical behavior can be seen as that of a fibre-reinforced composite material. TDBS experiments showed that the high transverse stiffness of a single-cell wall, in the direction perpendicular to the epidermis layer, is due to the strong bonding of microfibrils by hemicelluloses.

The micro-rheology of the nucleus of mammalian cells was explored at GHz frequencies with TDBS [49]. As for BLM and other experimental techniques, the results are consistent with a model that considers heterogeneous scaffolds of chromatin fibres with diverse globular conformations and concentration as the main load-bearing component, bathed in an interstitial cytosol-like fluid [11,50]. The large number of conformations of the nuclear components at various length scales yields a multiplicity of relaxation times and leads to a weak power-law rheology [13] resembling that found in polymer networks [51]. In this study, the attenuation we derived at high frequencies for osteosarcoma gives a longitudinal loss tangent for control cells of $\tan\delta = M'/M'\prime \approx 0.06$ only. This low value of the loss tangent is consistent with our previous observations, in several types of mammalian cells, of an intra-nuclear behavior similar to that of a solid glass at GHz frequencies.

The phonon wavelength in TDBS experiments $\lambda/2n \approx 140$ nm is longer than the characteristic length of the fibres and interstices, so homogenization theory applies to describe the mechanical behavior we are probing [49]. In this context, the network and fluid behave as an iso-strain two-phase system of which the effective storage modulus can be obtained by a Voigt average of the moduli of the network and of the fluid, weighted by their respective volume fractions. To give numbers, the storage modulus, as probed by classic Brillouin light scattering, is typically $M'_{DNA} \approx 8$ GPa for DNA, as for most proteins [52], and can reach $M'_{gp} \approx 22$ GPa for dry globular proteins [53]. Considering that the network is stiffer than the fluid, the effective modulus is approximated with $M' = \varnothing M'_n$, where $\varnothing$ and M'_n denote the volume fraction and storage modulus of the solid chromatin network. Considering that M'_n cannot be larger than M'_{gp} the value for effective M' we measured for control cells, Fig. 3, gives a plausible value for the volume fraction of the chromatin network of ≥ 0.6 [15]. These results, together with previous studies [49] confirm a view of the nucleus as a solid network of chromatin and other intra-nuclear components bathed in a cytosol-like fluid, rather than a homogeneous viscous compartment [50]. In this context, the effective storage modulus we are measuring depends primarily on the stiffness of the DNA chains [54], on the conformation of their packing with proteins, and on the concentration of the chromatin fibres they form. This asset makes TDBS a suitable means to probe changes in the intra-nuclear mechanical properties.

The mechanical changes we imaged are not caused by DNA damage directly but by the molecular structural changes the cell triggers in the nucleus volume to promote damage signaling and repair. Thus although the size of the damage foci could be submicron the in-plane resolution of the TDBS measurements, ≈ 1 μm in this work that could be improved using a shorter light wavelength or a higher magnification, is suited to explore the inhomogeneity of the cell response to exposures to DNA damaging agents.

As mentioned previously, exploration of the cell response to DNA damaging agents requires statistical analysis over a large number of experimental data, of which the acquisition is made possible by fixing cells after exposure. Cell mechanics and dynamics are mediated by protein motions that occur on time scales greater than typical relaxation times of the order of milliseconds [55]. Fixation with aldehydes may hamper the movements of these proteins within cells hence impacting on the mechanical response of cells to dynamic solicitations at frequencies less than kHz. At higher GHz frequencies, relaxation hinders the motion of these proteins. The cell behavior approaches that of a solid, with a storage modulus typically in the GPa range, and it is dominated by structural conformations [55]. These conformations do not evolve with fixation. This was confirmed with Brillouin spectroscopy performed with live and fixed HeLa cells showing a maximum increase of the Brillouin shift of only 4.9 % for fixed cells compared to live counterparts [56]. Interestingly moreover, it was found that the frequency ratio of the fixed and live cells is the same in the cytoplasm, nucleus and nucleoli meaning that it does not depend on the nano-structuration, thus this ratio should neither depend on the chromatin condensation in particular. It is therefore consistent to consider that the differential in nucleus' mechanical properties we are measuring in fixed conditions is significant of the differential that would be measured with in vitro conditions.

4.2. Changes in the intra-nucleus mechanics following DNA damage by MMS

Given the previous conclusions, it is clear that the TDBS results reveal changes in the intra-nucleus nanostructure. Deciphering which nano-structural changes, among those listed above, are predominant would however require complementary molecular imaging analysis or coupling with numerical models dedicated to the mechanics of the cell nucleus. Nevertheless, discussion of our TDBS results together with immunodetection observations enables us to identify connections between the changes in the intra-nucleus mechanical properties we measured and the nanostructure changes the cell activates when the damaging agent is applied, or after.

The changes in the storage modulus M' of the cells in the first group reveal changes in the intra-nucleus nanostructure that strongly soften the nucleus. We believe that the mechanical changes may not arise directly from DSBs but rather from events that they trigger and that affect the nuclear mechanics further downstream [9]. As mentioned in literature and summarized above, the softening of the load-bearing scaffold can be related to changes in the conformation of DNA packing by the histone proteins that result in a softening of the chromatin fibers, or a decrease in the concentration of chromatin fibers [3,4,7,9,17,54].

Such structural changes favor the recruitment of repair and checkpoint protein complexes in the chromatin microenvironment surrounding the DNA damage and support the active repair of DNA damage [9].

The cell-by-cell analysis, see SI, gives access to the spatial spreading of the softening within cells, and to a comparison of softening from one cell to another. This suggests that on average the damage, as revealed by stiffness decrease, is uniform inside each cell nucleus for all exposure times. In addition, this shows first that the softening effect is nearly the same for all cells when samples are exposed to MMS for a short time, 30 min. Second, our analysis shows that for a longer exposure time, 1 h, some cells were more susceptible to a further increase in the softening caused by DNA damage than others. This is consistent with the increase in the standard deviation of the number of damage foci per cell shown in our preliminary immunodetection experiments, Fig. 2b.

The changes in the loss tangent M''/M' reveal a change in acoustic dissipation. In polymers, this is a consequence of local segmental motion and of polymeric chain modes both contributing to the dynamics relaxation in the region of the considered acoustic spectrum [57]. The large increase, by 22 ± 12 % [35], in the mean of acoustic loss tangent that we measured in the nuclei of cells in the first group reveals a large increase in the acoustic dissipation processes. This can result from an increased number of segmental complexes of a similar size to the acoustic wavelength we are probing, ≈ 140 nm, possibly chromatin bundles or clustering of proteins at the damage foci [58]. Damaged ends are indeed surrounded by many proteins forming the repair focus [59]. This compartment is more than 50 times more concentrated in some repair proteins (Rad52) compared to undamaged cells [60]. In addition, checkpoint proteins bind to the phosphorylated histone **H2A.X** [61]. Such clustering also favours dissipation of the CAPs energy.

Increased dissipation can also be caused by changes in the flexural rigidity of chromatin fibers, making their flexural modes match the acoustic spectrum. It has indeed been reported that changes in the chromatin fiber flexional rigidity are scale-dependent [10] and can have several causes. On the one hand, histone eviction from the chromatin at the damaged sites, facilitating the recruitment of repair factors, increases the fibers' flexibility [5]. On the other hand, histone **H2A** phosphorylation may explain global chromatin flexional stiffening throughout the genome after local DSB damage, as reported in recent studies of chromatin dynamics in yeast [8]. Local flexional stiffening can also be caused by the proteins recruited to repair the DSB. Notably, it has been shown that the presence of Rad51 at the broken ends rigidifies DNA at the break [10].

These nano-structure changes are consistent with those mentioned previously in this section that possibly cause the decrease in the storage modulus M'. It is also worth noting that the kinetics of protein recruitment at the DNA breaks is of the order of minutes [62], less than the minimum exposure time we considered for the TDBS evaluation. The changes with the exposure time of M' that we measured must thus be attributed to the increasing number of DSBs and to chromatin decondensation rather than to the dynamics of the protein recruitment at the DNA breaks.

4.3. Opposite mechanical response when cells recover

Interestingly, the reverse evolution was measured when the damaging agent, MMS, was removed and cells were incubated for two hours in the buffer medium before fixation. An increase in the storage modulus M' with respect to the control sample was measured and this change increases with the exposure time to MMS. Having in mind that the storage modulus decreases with exposure to MMS, see above, the changes in the storage modulus over 2 h, *i.e.* with respect to the damaged cells, is even greater. We measured that the mean storage modulus increased by 14 ± 3 % [35] after exposure to MMS for 3 h, see Fig. 4a and data shown with red labels in Fig. 3a and Fig. 3d. The increase in the storage modulus could be related to the stiffening of the chromatin fibre as a mechanism underlying increased chromatin mobility [10]. This stiffening could also be considered in light of the interplay of internal nuclear components with the intracellular microenvironment. For instance, a significant increase in the longitudinal modulus of the nucleus was measured when cells are treated with nocodazole, which is known to disrupt microtubules, indicating that nuclear mechanics can be affected by the cytoskeletal behavior [46].

The cell-by-cell analysis of the spatially resolved data, see SI, suggests that recovery was not homogenous inside each nucleus and that zones of dense chromatin scaffold were firstly stiffened. Where there is more chromatin seems to be where the response to damage is more active. Moreover, inside a group of cells exposed for a short time, our data suggest that cells with the softer nucleus, *i.e.* with the greater effect of damage in terms of chromatin decondensation, are cells where stiffening during recovery is greater. For long exposure times, the recovery, as revealed by the increase in the storage modulus, seems to be the same for all nuclei.

Because the storage modulus retrieved after 2 h′ recovery is higher than for the control cells, re-stiffening of the chromatin fibres and re-condensation of the chromatin scaffold are probably not the only processes in play. Because the mean value of nucleus thickness does not decrease we also excluded shrinking of the chromatin scaffold, despite the fact that it could explain abnormal chromatin condensation. Cell death was also excluded because the cells still adhered to the titanium layer, otherwise TDBS measurements could not be achieved. In addition, the staining of nuclei with Hoechst^{33342} revealed no DNA condensation, Fig. 2a, suggesting the absence of apoptosis [63].

4.4. Two competitive responses

The dimensionless relative change in the storage modulus is a key internal variable to describe damage mechanics in solids [64]. Here, it is representative of the density of damage or repair activity regardless of the initial chromatin density or chromatin stiffness, and it is shown with red lines in Fig. 4. We hypothesize that the changes in M' are the result of competitive processes with opposite effects. Once MMS had diffused to DNA, DSB yielded chromatin decondensation and changes in chromatin conformation that caused the decrease in the chromatin density and stiffness, resulting in a decrease in the mean storage modulus, as we plotted with the red line in Fig. 4a. The subsequent recruitment of proteins at the DSB foci, such as DNA damage checkpoint factors, DNA repair factors, and chromatin modulators, seems to provoke stiffening of the interior of the nucleus, as shown with the red line in Fig. 4b, since after MMS was rinsed and MMS had diffused to chromatin the repair activity remains primarily.

We thus infer that the damaging effect caused by changes to chromatin is greater during MMS exposure than the one we measured, red lines in Fig. 4a, because it was counter-balanced by the stiffening associated with protein recruitment. The relative dynamics and magnitude of these two processes with opposite effects yield a maximum decrease in the storage modulus at one-hour exposure, with saturation afterwards implying no change or only minor change in the storage modulus. These dynamics are consistent with the changes in foci number as quantified by the immunostaining of **γH2A.X**, Fig. 2b.

The relative changes in mean nucleus thicknesses we measured, see

Section 3.1 and SI, also show opposite tendencies. We measured an increase of 16 ± 13 % [35] in relative mean thickness when cells were exposed for 30 min, which was not detected when cells were exposed for longer. This means that the nucleus expands during the first exposure period and contracts afterwards, still during the exposure. Interestingly, an opposite relative decrease was measured when cells exposed for 30 min had recovered for 2 h. During recovery also, the nucleus actively recovers its initial thickness.

Osmotic nuclear swelling following damage-induced inflammation is a mechanism that was reported recently [15,65]. The nucleus thickness changes and the dynamics we measured could be correlated with this signalling process. A clear connection would however require further investigation with B-POM since swelling/unswelling could also be caused by metabolic changes induced by cellular stresses mediated by media rinsing or temperature changes.

The relative changes in the loss tangent we plotted with blue lines in Fig. 4 are representative of the evolution of the sources for acoustic dissipation at a wavelength of ≈ 140 nm. The increase of dissipation sources follows the same pattern during exposure as the decrease in the storage modulus. This suggests that at least part of dissipation is related to chromatin changes that cause a decrease in the storage modulus, such as chromatin decondensation, changes in chromatin conformation and stiffness. We noticed, however, that for a short exposure time, 30 min, the increase in dissipation sources was still active during recovery, while the decrease in the storage modulus was not, which suggests that other dissipation sources are active in this case during recovery.

5. Conclusions

DNA is vital for nearly all cellular processes and must consequently be repaired when damaged. To do this, mammalian cells have evolved genome maintenance strategies that are appropriately mobilized. At present, it remains unknown how DNA damage response is functionally linked to the nuclear architecture and chromatin organization. We validated TDBS as a label-free method for the remote characterization of intra-nuclear mechanics. We observed mechanical changes in the nucleus due to the epigenetic modulation of nanoscale nuclear components. We found different types of behavior during exposure to the DNA damaging agent and after it was removed. We attributed the changes in storage modulus to the cumulative effect of opposite tendencies. Softening, initiated at MMS exposure, can be subsequent to chromatin decondensation and to changes in chromatin conformation that favor the recruitment of repair and checkpoint proteins in the chromatin microenvironment. This is counter-balanced by apparent stiffening of the interior of the nucleus caused by the later recruitment of these proteins. The changes in chromatin flexibility and molecular crowding are also probed with the changes of the loss modulus we measured intra-nucleus.

With its ability to probe the intra-nuclear mechanics, time-domain Brillouin microscopy opens up new avenues for research aiming at deciphering the mechanisms involved in the cell's response to DNA damage. It will notably be of interest to determine the mechanisms through which nuclear mechanics influence DNA damage levels, as this would influence therapeutic resistance. It will be of complementary interest to dissect the mechanism by which DNA damage response dictates changes in the nuclear mechanics that opens pathways to signalling and repair proteins, as it would influence therapeutic access to the genome.

Author contributions

B.A., P.B. and H.S. conceived and coordinated the project. **L.L., M. S., G.M., P.B., H.S.** and **B.A** discussed cell samples. **M.S., G.M., P.B.** and **H.S.** cultured the osteosarcoma cells, grafted and fixed these cells onto the Ti samples. **MA, GK, JC** managed and performed irradiation experiments in medical facilities at the Medical Physics Unit at Institut Bergonié . MMS exposure conditions and experiments were optimized and performed by **M.S., G.M.** Radiation biology experiments were performed by **FV, M.S.** and **G.M. L.L.** carried out the opto-acoustic experiments and processed the data. **L.L.** and **B.A.** wrote the manuscript. All authors commented on the manuscript..

Declaration of Competing Interest

The authors declare that they have no known competing financial interests or personal relationships that could have appeared to influence the work reported in this paper.

Data availability

Data will be made available on request.

Acknowledgements

L. L., and B.A. acknowledge financial support from the Agence Nationale de la Recherche (grant ANR-17-CE11-0020-01), from the Region Nouvelle-Aquitaine (grant 2016-1R-60301). All authors acknowledge the financial support from the POPRA and FEDER programs, and from the Université de Bordeaux. L.L. acknowledges financial support from Suzhou Ecological and FWO, France postdoctoral research fellowship (12V4419N).

Appendix A. Supporting material

Supplementary information: details of the processing of the opto-acoustic signals and cell-by-cell analysis of the numerous data acquired for each group of cells.

Online movie: dynamic reflectivity changes, measured at a nanosecond time scale, of a single nucleus.

Appendix B. Supporting information

Supplementary data associated with this article can be found in the online version at doi:10.1016/j.pacs.2022.100385.

References

[1] S.P. Jackson, J. Bartek, The DNA-damage response in human biology and disease, Nature 461 (2009) 1071–1078.
[2] T. Helleday, J. Lo, D.C. van Gent, B.P. Engelward, DNA double-strand break repair: from mechanistic understanding to cancer treatment, DNA Repair 6 (2007) 923–935.
[3] M.H. Hauer, S.M. Gasser, Chromatin and nucleosome dynamics in DNA damage and repair, Genes Dev. 31 (2017), 2204-2201.
[4] N.C.M. House, M.R. Koch, C.H. Freundenreich, Chromatin modifications and DNA repair: beyond double-strand breaks, Front. Genet. 5 (2014) 296.
[5] M. Hauer, A. Seeber, V. Singh, R. Thierry, R. Sack, A. Amitai, M. Kryzhanovska, J. Eglinger, D. Holcman, T. Owen-Hughes, S.M. Gasser, Histone degradation in response to DNA damage enhances chromatin dynamics, and recombination rates, Nat. Struct. Mol. Biol. 24 (2017) 99.
[6] J. Miné-Hattab, I. Chiolo, Complex chromatin motions for DNA repair, Front. Genet. 11 (2020) 800.
[7] A. Dos Santos, C.P. Toseland, Regulation of nuclear mechanics and the impact on DNA damage, Int. J. Mol. Sci. 22 (2021) 3178.

[8] S. Herbert, A. Brion, J.-M. Arbona, M. Lelek, A. Veillet, B. Lelandais, J. Parmar, F. G. Fernández, E. Almayrac, Y. Khalil, E. Birgy, E. Fabre, C. Zimmer, Chromatin stiffening underlies enhanced locus mobility after DNA damage in budding yeast, EMBO J. 36 (17) (2017) 2595–2608.

[9] A. Dos Santos, A.W. Cook, R.E. Gough, M. Schilling, N.A. Olszok, I. Brown, L. Wang, J. Aaron, M.L. Martin-Fernandez, F. Rehfeldt, C.P. Toseland, DNA damage alters nuclear mechanics through chromatin reorganization, Nucleic Acids Res. 49 (1) (2021) 340–353.

[10] J. Miné-Hattab, V. Recamier, I. Izeddin, R. Rothstein, X. Darzacq, Multi-scale tracking reveals scale-dependent chromatin dynamics after DNA damage, Mol. Biol. Cell 28 (23) (2017) 3323–3332.

[11] M. Zwerger, C.Y. Ho, J. Lammerdin, Nuclear mechanics in disease, Annu. Rev. Biomed. Eng. 13 (1) (2011) 397–428.

[12] J.D. Pajerowski, K.N. Dahl, F.L. Zhong, P. Zammak, D.E. Discher, Physical plasticity of the nucleus in stem cell differentiation, Proc. Nat. Acad. Sci. USA 104 (40) (2007) 15619–15624.

[13] K.N. Dahl, A.J. Engler, J.D. Pajerowski, D.E. Discher, Power-law rheology of isolated nuclei with deformation mapping of nuclear substructures, Biophys. J. 89 (2005) 2855–2864.

[14] A.D. Stephens, E.J. Banigan, S.A. Adam, R.D. Goldman, J.F. Marko, Chromatin and lamin A determine two different mechanical response regimes of the cell nucleus, Mol. Biol. Cell 28 (2017) 1984–1996.

[15] Y. Xia, C.R. Pfeifer, S. Cho, D.E. Discher, J. Irianto, Nuclear mechanosensing, Emerg. Top. Life Sci. 2 (5) (2018) 713–725.

[16] A. Mazumder, T. Roopa, A. Basu, L. Mahadevan, G.V. Shivashankar, Dynamics of chromatin decondensation reveals the structural integrity of a mechanically prestressed nucleus, Biophys. J. 95 (2008) 3028–3035.

[17] J. Zhang, X.A. Nou, H. Kim, G. Scarcelli, Brillouin flow cytometry for label-free mechanical phenotyping of the nucleus, Lab Chip 17 (2017) 663–670.

[18] H. Strickfaden, T.O. Tolsma, A. Sharma, D.A. Underhill, J.C. Hansen, M.J. Hendzel, Condensed chromatin behaves like a solid on the mesoscale in vitro and in living cells, Cell 183 (2020) 1772–1784.

[19] H. Liu, J. Wen, Y. Xiao, J. Liu, S. Hopyan, M. Radisic, C.A. Simmons, Y. Sun, In situ mechanical characterization of the cell nucleus by atomic force microscopy, ACS Nano 8 (4) (2014) 3821–3828.

[20] B.T. Bennett, Immunofluorescence imaging of DNA damage response proteins: optimizing protocols for super-resolution microscopy, Methods 48 (2009) 63–71.

[21] C.A. Schneider, W.S. Rasband, K.W. Eliceiri, NIH image to ImageJ: 25 years of image analysis, Nat. Methods 9 (7) (2012) 671–675.

[22] C. Thomsen, H.T. Graham, H.J. Maris, J. Tauc, Picosecond interferometric technique for study of phonons in the Brillouin frequency range, Opt. Commun. 60 (1986) 55–58.

[23] V.E. Gusev, P. Ruello, Advances in applications of time-domain Brillouin scattering for nanoscale imaging, Appl. Phys. Rev. 5 (2018), 031101.

[24] C. Thomsen, J. Strait, Z. Vardeny, H.J. Maris, J. Tauc, J. Hauser, Coherent phonon generation and detection by picosecond light pulses, Phys. Rev. Lett. 53 (1984) 989–992.

[25] L. Brillouin, Diffusion de la lumière et des rayons X par un corps transparent homogène; influence de l'agitation thermique, Ann. Phys. 17 (1922) 88–122.

[26] L.I. Mandelstam, Light scattering by inhomogeneous media, Zh. Russ. Fiz. Khim. Ova. 58 (1926) 381–385.

[27] Z. Meng, A.J. Traverso, C.W. Ballman, M.A. Troyanova-Wood, V.V. Yakovlev, Seeing cells in a new light: a renaissance of Brillouin spectroscopy, Adv. Opt. Photonics 8 (2) (2016) 300–327.

[28] F. Palombo, D. Fioretto, Brillouin light scattering: applications in biomedical sciences, Chem. Rev. 119 (13) (2019) 7833–7847.

[29] A. Bartels, F. Hudert, C. Janke, T. Dekorsy, K. Köhler, Femtosecond time-resolved optical pump-probe spectroscopy at kilohertz-scan-rates over nanosecond-time-delays without mechanical delay line, Appl. Phys. Lett. 88 (4) (2006) 1–3.

[30] The refractive index and mass density we considered for osteosarcoma are n = 1.35 and $\rho = 1.1\ g.cm^{-3}$.

[31] D.T. Beranek, Distribution of methyl and ethyl adducts following alkylation with monofunctional alkylating agents, Mutat. Res. 231 (1990) 11–30.

[32] T. Lindahl, R.D. Wood, Quality control by DNA repair, Science 286 (1999) 1897–1905.

[33] L.C. Riches, A.M. Lynch, N.J. Gooderham, Early events in the mammalian response to DNA double-strand breaks, Mutagenesis 23 (5) (2008) 331–339.

[34] R. Galen, A. Shoracket Jon, Wellner, Empirical processes with applications to statistics, John Wiley& Sons Inc, 1986. ISBN 047186725X.

[35] See SI for data value and estimation of uncertainty.

[36] L. Liu, A. Viel, G. Le Saux, L. Plawinski, G. Muggiolu, P. Barberet, M. Pereira, C. Ayela, H. Seznec, M.C. Durrieu, J.M. Olive, B. Audoin, Remote imaging of single cell 3D morphology with ultrafast coherent phonons and their resonance harmonics, Sci. Rep. 9 (2019) 6409.

[37] G.N. Papanicolaou, H.F. Traut, The Diagnostic value of vaginal smears in carcinoma of the uterus, Am. J. Obstet. Gynecol. 42 (1941) 193–206.

[38] D. Pranab, Cancer nucleus: morphology and beyond, Diagn. Cytopathol. 38 (5) (2010) 382–390.

[39] We measured M' =12.6 GPa for cells from the control sample and M' =13.9 GPa for cellsexposed to X-Rays and fixed 2 hours after. Same uncertainty as for MMS exposure wasattributed to these measurements.

[40] R. Prevedel, A. Diz-Munoz, G. Ruocco, G. Antonacci, Brillouin microscopy: an emerging tool for mechanobiology, Nat. Methods 16 (2019) 969–977.

[41] J. Zhang, G. Scarcelli, Mapping mechanical properties of biological materials via an add-on Brillouin module to confocal microscopes, Nat. Protoc. 16 (2021) 1251–1575.

[42] Z. Meng, T. Thakur, C. Chitrakar, M.K. Jaiswal, A.K. Gaharwar, V.V. Yakovlev, Assessment of local heterogeneity in mechanical properties of nanostructured hydrogel networks, ACS Nano 11 (2017) 7690–7696.

[43] G. Scarcelli, W.J. Polacheck, H.T. Nia, K. Patel, A.J. Grodzinsky, R.D. Kamm, S. H. Yun, Noncontact three-dimensional mapping of intracellular hydromechanical properties by Brillouin microscopy, Nat. Methods 12 (2015) 1132–1134.

[44] E.H. Zhou, X. Trepat, C.Y. Park, G. Lenormand, M.N. Oliver, S.M. Mijailovich, C. Hardin, D.A. Weitz, J.P. Butler, J.J. Fredberg, Universal behavior of the osmotically compressed cell and its analogy to the colloidal glass transition, Proc. Natl. Acad. Sci. USA 106 (2009) 10632–10637.

[45] G. Antonacci, S. Braakman, Biomechanics of subcellular structures by non-invasive Brillouin microscopy, Sci. Rep. 6 (2016) 37217.

[46] J. Zhang, F. Alisafaei, M. Nikolić, X.A. Nou, H. Kim, V.B. Shenoy, G. Scarcelli, Nuclear mechanics within intact cells is regulated by cytoskeletal network and internal nanostructures, Small 16 (18) (2020), 1907688.

[47] K.F. Toth, T.A. Knoch, M. Wachsmuth, M. Frank-Stöhr, M. Stöhr, C.P. Bacher, G. Müller, K. Rippe, Trichostatin A-induced histone acetylation causes decondensation of interphase chromatin, J. Cell Sci. 117 (2004) 4277–4287.

[48] A. Gadalla, T. Dehoux, B. Audoin, Transverse mechanical properties of cell walls of single living plant cells probed by laser-generated acoustic waves, Planta 239 (2014) 1129–1137.

[49] O.F. Zouani, T. Dehoux, M.-C. Durrieu, B. Audoin, Universality of the network-dynamics of the cell nucleus at high frequencies, Soft Matter 10 (2014) 8737–8743.

[50] M. Wachsmuth, W. Waldeck, J. Langowski, Anomalous diffusion of fluorescent probes inside living cell nuclei investigated by spatially-resolved fluorescence correlation spectroscopy, J. Mol. Biol. 298 (2000) 677–689.

[51] Y. Tseng, J.S.H. Lee, T.P. Kole, I. Jiang, D. Wirtz, Micro-organization and visco-elasticity of the interphase nucleus revealed by particle nanotracking, J. Cell Sci. 117 (215) (2004) 2167.

[52] S.A. Lee, S.M. Lindsay, J.W. Powell, T. Weidlich, N.J. Tao, G.D., A. Lewen, A. Rupprecht, Brillouin scattering study of the hydration of Li- and Na-DNA films, Biopolymers 26 (1987) 1637–1665.

[53] S. Speziale, F. Jiang, C. Caylor, S. Kriminski, C.-S. Zha, R. Thorne, T. Duffy, Sound velocity and elasticity of tetragonal lysozyme crystals by Brillouin spectroscopy, Biophys. J. 85 (2003) 3202–3213.

[54] Y. Shimamoto, S. Tamurad, H. Masumotoe, K. Maeshima, Nucleosome–nucleosome interactions via histone tails and linker DNA regulate nuclear rigidity, Mol. Biol. Cell 28 (2017) 1580–1589.

[55] D. Stamenovic, Cell Mechanics: two regimes, maybe three? Nat. Mater. 5 (2006) 597–598.

[56] G. Antonacci, V. de Turis, A. Rosa, G. Ruocco, Background-deflection Brillouin microscopy reveals altered biomechanics of intracellular stress granules by ALS protein FUS, Comm. Biol. 1 (2018) 139.

[57] D. Fioretto, F. Scarponi, Dynamics of a glassy polymer studied by Brillouin light scattering, Mater. Sci. Eng. A 521 (2009) à243–à246.

[58] H. Tadayyon, M.J. Gangeh, R. Vlad, M.C. Kolios, G.J. Czarnota, Ultrasound imaging of DNA-damage effects in live cultured cells and in brain tissue, in: Vladimir V. Didenko (Ed.), Fast Detection of DNA Damage: Methods and Protocols, Methods in Molecular Biology, 1644, © Springer Science+Business Media LLC, 2017, https://doi.org/10.1007/978-1-4939-7187-9_3.

[59] M. Lisby, J.H. Barlow, R.C. Burgess, R. Rothstein, Choreography of the DNA damage response: spatiotemporal relationships among checkpoint and repair proteins, Cell 118 (2004) 699–713.

[60] M. Lisby, R. Rothstein, Cell biology of mitotic recombination, Cold Spring Harb. Perspect. Biol. 7 (2015), a016535.

[61] I.M. Ward, K. Minn, K.G. Jorda, J. Chen, Accumulation of checkpoint protein 53BP1 at DNA breaks involves its binding to phosphorylated histone H2A.X, J. Biol. Chem. 278 (22) (2003), 19579-15582.

[62] S.E. Polo, S.P. Jackson, Dynamics of DNA damage response proteins at DNA breaks: a focus on protein modifications, Genes Dev. 25 (5) (2011) 409–433.

[63] Crowley, L.C., Marfell, B.J., Waterhouse, N.J., Analysing Cell Death by Nuclear Staining with Hoechst33342, Cold Spring Harb Protoc. ⟨https://doi.org/10.1101/pdb.prot087205⟩.

[64] J.S. Baste, B. Audoin, On internal variables in anisotropic damage, Eur. J. Mech., A Solids 10 (5) (1991) 1–20.

[65] B. Enyedi, M. M. Jelcic, P. Niethammer, The cell nucleus serves as a mechanotransducer of tissue damage-induced inflammation, Cell 165 (5) (2016) 1160–1170.

Bertrand Audoin works as Professor at Université de Bordeaux, France. He was involved in laser ultrasonics and their applications to the non-destructive evaluation of anisotropic materials. The research led in his group also focused on picosecond ultrasonics. They have performed the acoustic diffraction in sub-micron sized solid samples and used absorption by a single particle as an opto-acoustic source. His current research focuses on picosecond bio-phononics: B. Audoin has demonstrated the first applications of picosecond ultrasonics to biologic media, a field totally unexplored at that time. His group has developed the opto-acoustic microscopy of single cells, an imaging modality where the mechanical prop erties are the contrast mechanism.

Liwang Liu received his Ph.D. degree in physics at KU Leuven, Belgium, in 2015. He is an experienced researcher in the field of photothermal and photoacoustic science. Dr. Liu developed activities concerning their applications to the non-destructive thermoelastic characterization of thin films, time-resolved spectroscopy of glassy dynamics in soft matter systems, and recently (since 2016) to the non-invasive and label-free imaging of the single-cell mechanics

Philippe Barberet is associate professor at the university of Bordeaux. He is working in Hervé Seznec's team at LP2I. His main expertize concerns experimental physics and his research focuses on the development of charged-particle microbeams and their applications to biology. In particular, P. Barberet has a long experience in targeted micro-irradiation of living cells with focused ion beams. He is the scientific coordinator of the particle accelerator at LP2I (AIFIRA Facility).

Hervé Seznec is research associate CNRS at Université of Bordeaux, France (LP2i, UMR5797). He received his doctorate (PhD) in Biology from the University of Paris, France in 2001. His area of research includes biology/genetics, biophysics and biochemistry. His current research interests focus on the development of cell irradiation and correlative cell imaging methodologies based on charged particle microbeam for studying the cellular stress responses of *in celluloid* and *in vivo* biological systems. One of the major objectives of his research is to address the cellular responses to ionizing radiation exposures using human cell culture or the nematode *C. elegans*.